Autogenous Pressurization of a Cryogenic Tank using Computational Fluid Dynamics

Bruce E. Ciccotosto[1] and Daniel M. Hauser[2]
NASA Glenn Research Center, Cleveland, OH 44135

Well-validated simulation tools can be used to predict long-term storage and transfer of cryogenic propellants, which are essential to NASA's mission plan to return to the Moon and continue to Mars. Autogenous pressurization of propellant tanks is used to supply rocket engine turbopumps with pressurized liquid fuel and oxidizer, preventing cavitation. Additionally, autogenous pressurization can be used to support on-orbit propellant transfer. In lieu of expensive tests conducted on-orbit, accurate predictive computational models of these processes can be used to reduce system and propellant mass as well as mission risk. Using simulation tools also reduces the cost of analyzing and developing this technology. This study presents a multiphase computational fluid dynamics model capable of simulating autogenous pressurization of a large cryogenic tank using the commercial code STAR-CCM+. Experimental data from a full-scale tank pressurization test under terrestrial gravity is compared to simulation results using transient error metrics. Comparisons show good agreement and give confidence in using these and other validated simulation tools to develop cryogenic pressurization systems.

I. Nomenclature

C_p	=	specific heat at constant pressure	$\dot{q}_{liq}$	=	energy source, liquid region
F	=	spatial filter function	R	=	universal gas constant
g	=	acceleration due to gravity	S_c, S_E	=	continuity, energy source term
k	=	thermal conductivity	T_{sat}	=	local saturation temperature
k_{eff}	=	effective thermal conductivity	T_{ref}	=	reference temperature
L	=	latent heat of vaporization	$\boldsymbol{u}$	=	velocity vector
M	=	molar mass	α	=	volume fraction
$\dot{m}_{vap}$	=	mass transfer rate in the vapor region	$β$	=	thermal expansion coefficient
$\dot{m}_{liq}$	=	mass transfer rate in the liquid region	$ε_m$	=	magnitude error coefficient
p	=	static pressure	$ε_p$	=	phase error coefficient
P_{vap}	=	absolute pressure of the vapor phase	$ε_c$	=	comprehensive error coefficient
P_{sat}	=	local saturation pressure	$ρ$	=	density
Q_{IL}	=	heat transfer from interface to vapor	$σ$	=	accommodation coefficient
Q_{IV}	=	heat transfer from interface to vapor	$ν$	=	kinematic viscosity
$\dot{q}_{vap}$	=	energy source, vapor region	$μ$	=	dynamic viscosity

II. Introduction

Long-term storage and transfer of cryogenic propellants are essential to NASA's mission plan to return to the Moon and continue onto Mars. Due to the large costs associated with cryogenic propellant system testing in low gravity environments, it is essential that simulation tools be developed to model and predict the behavior of these systems under terrestrial and low gravity conditions. Well-validated computational tools such as Computational Fluid Dynamics (CFD) can be used to predict the performance of these systems prior to flight testing thus reducing the mission cost and risk. Pressurization of the propellant tank is a commonly used method to provide cryogenic propellant

---

[1] Associate Researcher, Fluid and Cryogenic Systems Branch
[2] Principal Engineer, Fluid and Cryogenic Systems Branch

to rocket engine turbopumps. To maintain pressure authority during operation, turbopumps require the propellant to be supplied above the saturation pressure of the propellant to prevent cavitation. Additionally, pressurization can also be used to support to on-orbit propellant transfer by using the ullage as a piston to push out the liquid phase. Autogenous pressurization is the use of the gaseous phase to pressurize the liquid phase within the propellant tank. A small amount of the liquid phase is removed from the tank, heated until converted to a gas, and then pumped back into the original tank. The vast increase in volume from changing phase from liquid to gas causes the ullage pressure to increase. Using autogenous pressurization has the benefit of not introducing inert gases to the ullage, reducing the cost of refueling and simplifying the design considerably. Additionally, the mass of gas pressurant needed can be quite significant, further justifying the use of chemical species already onboard the spacecraft [1]. The increase in pressure can cause condensation of the ullage, increasing the pressurant mass needed. Ambient heat leaks through walls or heat transfer from the pressurant can also cause evaporation depending on the internal fluid dynamics. It is therefore important to develop a predictive model that can account for the fluid motion, thermodynamics, and phase interactions of the two-phase system. In the present work, nitrogen autogenous pressurization of the Engineering Development Unit (EDU) tank under terrestrial gravity is simulated using a multiphase model developed for the commercial CFD software STAR-CCM+ [2]. Simulated results are compared to experimental values using transient error metrics, which provide a robust method of comparing multiple series of data.

III.   Experimental Background

The EDU tank has an internal volume of 4250 liters with a maximum internal radius of 850 mm, an internal maximum height of 2350 mm and consists of cryogenic grade aluminum alloy 2219 (AL2219). The tank consists of several inflow and outflow paths and various instrumentation. The tank was insulated with 25.4 mm of foam, and 60 layers of multi-layer insulation. Testing was conducted in vacuum conditions and approximately 300K ambient temperature. As of 2021, there is no final testing report on this tank or the testing conducted, but some experimental data and documentation is available publicly [3],[4]
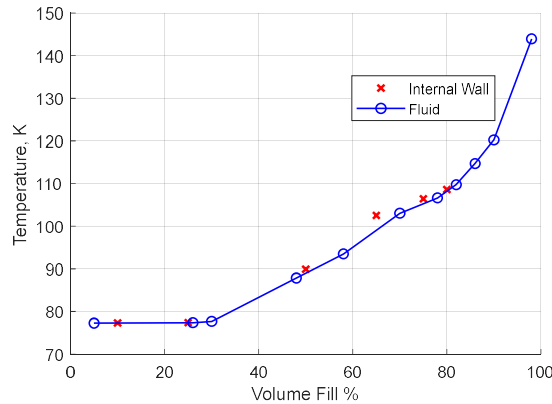

Fig. 1 Initial temperature profiles from experiment.

The test case considered is filled with liquid nitrogen (LN2) at 25% volume, and the remaining tank volume is gaseous nitrogen (GN2). In the test considered, GN2 is added through an ullage diffuser roughly along the central axis of the tank and 220 mm from the top of the tank. The tank is initially quiescent and under terrestrial gravity. The initial temperature profile of the tank is shown in Fig. 1.

During the test, the tank was vented to atmospheric conditions and the LN2 and GN2 were left to reach saturation conditions. After this, gaseous nitrogen was pumped into the tank through the ullage diffuser, raising the internal pressure over time. This autogenous N2 pressurization test lasted for 2000 seconds. For simulation purposes, the relevant experimental instrumentation includes the inlet mass flow, ullage and liquid temperature rakes, and pressure sensors.

IV. Simulation Setup

The ullage diffuser consists of a 4-inch diameter can covered with 2 mm drilled holes and surrounded by a fine mesh screen. Given the scale of the tank and the length of the experiment, resolving the diffuser flow scales and the overall pressure trace of the tank using CFD is impractical. Thus, the diffuser is assumed to be in the center of the tank along the central axis and mass flow to be uniform and normal to the inlet surface. The diffuser inlet temperature and mass flow rate varied are over time according to the experiment and is presented in Fig. 2. The main boundary conditions are shown in Fig. 3, all other boundaries are adiabatic walls. The outer walls of the tank are assumed
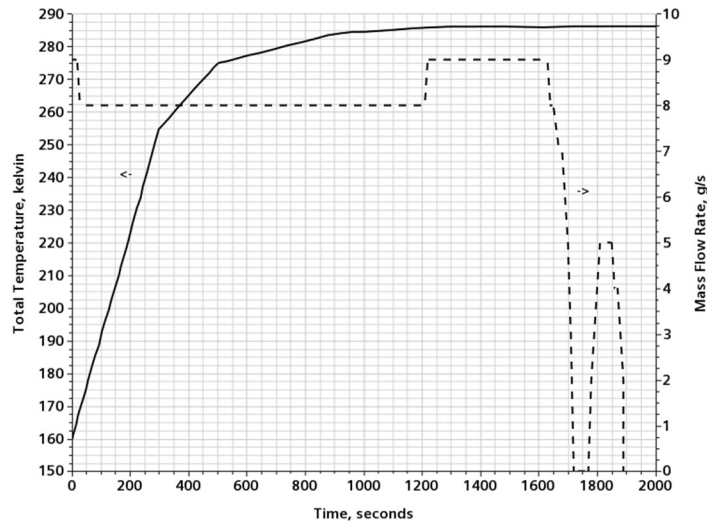

Fig. 2 Inlet conditions.

adiabatic as the experiment was highly insulated, and heat leak was considered negligible. The internal geometry of the tank was simplified to allow the use of a 2D axisymmetric model. Various brackets, wires, pipes, and instrumentation are mounted to the top of the tank that likely affect the local fluid motion, but not the overall tank pressurization signature. The diffuser hardware also adds some thermal mass to the system, but as the inlet flow is
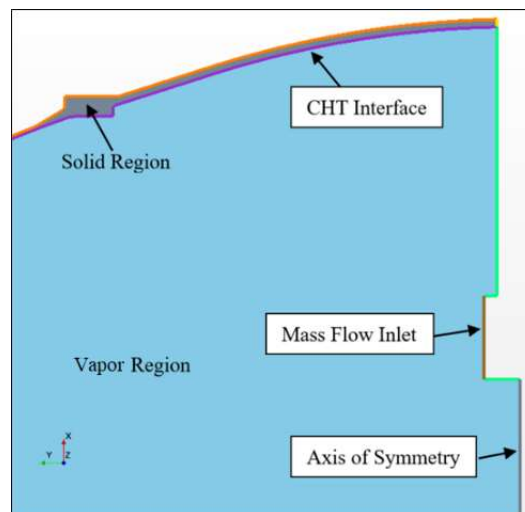

Fig. 3 CFD boundary conditions.

already simplified greatly, resolving the CHT to the diffuser housing has no value. The resulting simulation domain is presented in Fig. 2, alongside the original tank geometry model. Dark blue represents the LN2 region, light blue is the GN2 region, and gray is the solid tank wall. A polynomial fit of the initial temperature profile was used as the initial condition for fluid and solid regions, as the difference was very slight. A polyhedral mesh is used with sizing

3

refinement near the liquid fill level, solid walls, and the diffuser inlet. The polyhedral mesh is the further refined with several prism layers on either side of the interface boundary. The solid walls of the tank add significant thermal mass and are linked by conjugate heat transfer (CHT) to the fluid domain, while the outer walls are adiabatic. A heat conduction model is used with constant material properties from Table 1 with a 2D axisymmetric spatial model.
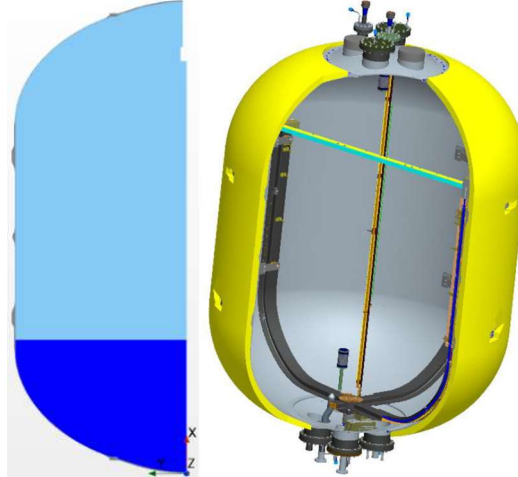

Fig. 2 Simulation domain and original tank geometry.

The fluid momentum, mass continuity, and energy are solved by discretizing the governing equations, and time integration is handled by the implicit unsteady model in STAR-CCM+. Fluid mass continuity and momentum are governed by the Navier-Stokes equations given in Eqs. (1)-(2), and the fluid energy is modeled with a transport equation in Eq. (3). Mass and energy transfer due to phase change are modeled by the source terms, S_c and S_E, in the mass continuity and energy equations respectively.

$$\frac{\partial \rho}{\partial t} + \nabla(\rho \boldsymbol{u}) = S_c \tag{1}$$

$$\frac{\partial (\rho \boldsymbol{u})}{\partial t} + \nabla(\rho \boldsymbol{u}\boldsymbol{u}) = -\nabla p + \nabla[\mu(\nabla \boldsymbol{u} + \nabla v^T)] + \rho g \tag{2}$$

$$\frac{\partial (\rho E)}{\partial t} + \nabla(\boldsymbol{u}(\rho E + p)) = \nabla(k_{eff}\nabla T) + S_E \tag{3}$$

Laminar and turbulent regimes were considered. For the turbulent cases, the k-ω Shear Stress Transport (SST) model was used. Material properties were taken from the National Institute of Standards and Technology REFPROP database and are listed in Table 1 [5]. Unless otherwise noted, all properties were assumed constant except the GN2 density which followed the ideal gas law.

Table 1   Material properties

	units	LN2	GN2	AL2219
ρ	$kg\ m^{-3}$	806	ideal gas	2702
μ	$Pa\ s$	1.6E-4	5.5E-6	-
c_p	$J\ kg^{-1}\ K^{-1}$	2040	1123.5	903
k	$Wm^{-1}K^{-1}$	0.145	0.0075	237
β	K^{-1}	0.0001	-	-
L	$kJ\ kg^{-1}$	199	-	-

A. Multiphase Model Formulation

The most common approaches to simulating multiphase flows are Eulerian multiphase (EMP), and volume of fluid (VOF). In EMP, two full sets of governing equations are solved for each fluid in a single region, additional closure relations are included as needed, and the two phases share a pressure field. In VOF, one set of governing equations is

solved for both phases, as well as volume fraction continuity, again in a single region and share a pressure field. The volume fraction is then used to weight material properties and field variables, giving the effect that there are two 'fluids' in the solution.

In the present work, a so-called sharp interface method (SI) developed by Kassemi et. al. is implemented in STAR-CCM+ for the first time [6]. The SI method is analogous to solving two single-phase regions simultaneously. In SI, one set of governing equations is solved for both single-phase regions and the fluids do not share a pressure field. Additionally, phase interaction is enforced by boundary conditions and not through additional closure relations. The sources and terms being evaluated can differ in each region (e.g. one region as ideal gas, the other as constant density), but the end result is solving the same governing equation across regions. This holds true because there are no terms in our governing equations that span across multiple regions. In other words, by solving two single phase regions, the number of equations to be solved does not increase, but the size of the matrices does, the same way matrices grow as the number of nodes increases. If we solve an additional equation in one region but not the other (e.g. helium diffusion in the vapor but neglect it in the liquid), the additional matrix is solved only in the necessary region. The popular VOF method is also used as benchmark for results from the SI method.

1. *Sharp Interface Method*

The internal volume of the tank is divided at the liquid-vapor interface where a wall boundary is placed. The saturation temperature is then calculated using the Clausius-Clapeyron relation from Eq. (4) and then enforced as a static temperature condition on the liquid side and vapor side of the interface boundary. This ensures that the interface is always at saturation condition.

$$T_{sat} = \left[\frac{1}{T_{ref}} - \frac{R}{LM} ln\left(\frac{P_{vapor}}{P_{ref}}\right) \right]^{-1} \tag{4}$$

The applied static temperature creates a heat flux due to a temperature gradient on both sides of the interface. While the interface nodes are always at saturation, the saturation condition changes with respect to time due to the pressure increase, therefore a nonzero gradient exists. The mass transfer rate is then calculated directly from an energy balance at the interface. The difference in heat fluxes divided by the latent heat gives the mass transfer between the two phases, and the magnitude of the mass continuity source as in Eq. (5).

$$S_c = \dot{m}_{vap} = \frac{Q_{IL} - Q_{IV}}{L} F_{vap} \tag{5}$$

Q_{IL} is the heat flux from the interface boundary to the liquid region, and Q_{IV} is the heat flux from the interface boundary to the vapor region. A spatial filter, F_{vap}, give values of one in cells adjacent to the interface in the vapor region and is zero elsewhere, to ensure sources are applied only near the interface. The mass source for the liquid region is neglected as the difference in densities is large. For a more thorough derivation, see the paper from Kassemi [6].

The energy sources for SI method are not the mass transfer and latent heat, $\dot{m}L$, but instead are the enthalpy content because the model is not changing phase in the simulation per se. In the case of evaporation, vapor mass is added to a region that contains only vapor and so the pressure increases. If the enthalpy content is not also added to this vapor region, the total energy in the vapor region remains constant, but with more mass therefore the temperature will reduce unphysically. The appropriate energy source is then the enthalpy of the added mass at the saturation temperature. It should be noted that STAR-CCM+ does not use a reference state when solving the energy equation, and the reference temperatures within the physics continua are for post-processing only and do not affect the solution. The energy sources can then be thought of as the 'absolute' enthalpy, or the enthalpy with a reference state at absolute zero. For the vapor region, this source is given by Eq. (6).

$$\dot{q}_{vap} = \dot{m}_{vap} C_{p_{vap}} T_{sat} \tag{6}$$

Note that the scalar field of $\dot{m}_{vap}$ is already filtered to the appropriate cells from Eq. (5). While the mass source in the liquid region is neglected, the enthalpy change in the liquid cannot be neglected as this modifies the temperature gradient near the interface. For the liquid region energy source, we must recalculate the mass transfer magnitude on the liquid side, which is simply the equal and opposite magnitude of Eq. (5) but filtered to the first adjacent liquid cell as in Eq. (7).

$$\dot{m}_{liq} = -\frac{Q_{IL} - Q_{IV}}{L} F_{liq} \tag{7}$$

As before, the appropriate energy source is the enthalpy of the mass undergoing phase change and is given in Eq. (8) using the liquid specific heat.

$$\dot{q}_{liq} = \dot{m}_{liq} C_{p_{liq}} T_{sat} \tag{8}$$

The overall source term for the energy equation is then the summation of Eqs. (6) and (8). There is a single S_E term in the SI formulation because the two single phase regions are solved simultaneously, and the governing equations span both regions. From Eq. (9), a discontinuous field of energy sources is given. In cells adjacent to the liquid interface it has values of the liquid phase energy source, in cells adjacent to the vapor interface it has values of the vapor energy source and is zero elsewhere.

$$S_E = \dot{q}_{vap} + \dot{q}_{liq} \tag{9}$$

The final ingredient to the SI model is creating a continuous velocity field between the regions. This allows momentum to transfer from one region to the other. To achieve this, the liquid-side interface is set as a slip wall. Again, we assume the difference in densities between phases is large and therefore the momentum of the vapor can be neglected compared to the liquid momentum. The velocity at the liquid-side slip wall is then imposed on the vapor side. This creates a continuous velocity field between the two phases. The boundary conditions at the interface and the source terms are then recalculated and reapplied after every timestep, and the two single phase regions can be solved simultaneously. The schematic in Fig. 3 summarizes the sharp interface setup in the cells nearest to the interface boundary for better visualization. For cases without mass transfer effects, all source terms were removed from the
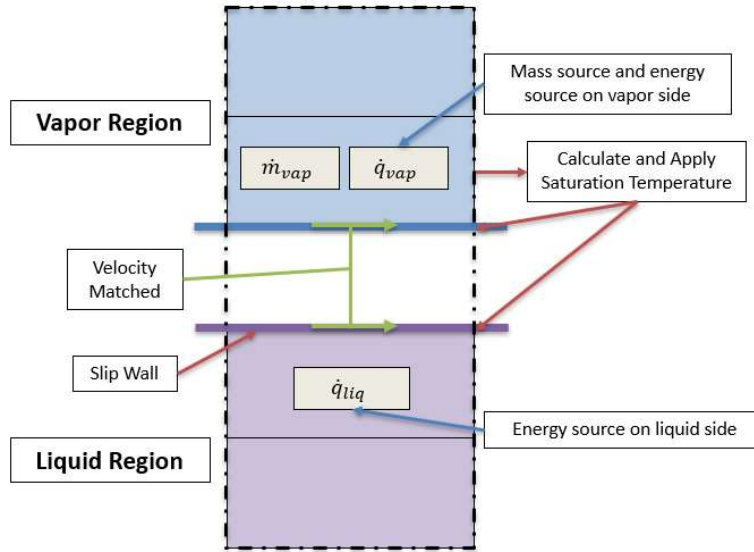

Fig. 3: Sharp Interface schematic in near the interface.

simulation, while the saturation temperature and liquid velocity were still enforced at the interface.

Splitting the solution domain in this way creates a much more stable CFD solution than the equivalent VOF setup. SI cases initially used a timestep of 1E-3 s, and this was gradually increased to as large as 0.125 s. This increase in timestep size had no impact on residual reduction at each timestep, and results were found to be timestep independent.

2. VOF method

The setup for VOF cases is largely the same as the previous SI cases, except of course that there is only fluid region in VOF. The governing equations are the same as before with the addition of the volume fraction continuity given in Eqn. (10).

$$\frac{1}{\rho_i} \left[\frac{\partial}{\partial t} (\alpha_i \rho_i) + \nabla (\alpha_i \rho_i v_i) = S_{\alpha_i} \right] \tag{10}$$

6

Where α_i is the volume fraction of the ith phase in each cell. Phase change and mass transfer at the liquid-vapor interface are modeled as source terms in the mass continuity, volume fraction continuity, and energy equations. Mass transfer rates were determined by the model from Schrage in Eq. (11), based in kinetic theory and near equilibrium conditions [7].

$$|\dot{\boldsymbol{m}}| = \left(\frac{2\sigma}{2-\sigma}\right)\left(\frac{M}{2\pi R}\right)^{1/2}\left(\frac{P_i}{T_i^{1/2}} - \frac{P_v}{T_v^{1/2}}\right) \qquad 11)$$

Here σ is the accommodation coefficient, taken as 1E-4; M is the molar mass of the fluid; R is the universal gas constant; P_i and P_{vap} are, respectively, the interfacial and vapor pressures; T_i and T_{vap} are the interfacial and vapor temperatures. It was assumed that $T_i = T_{vapor} \cong T_{sat}$ at the interface and that $P_i \cong P_{sat}$. This simplification yields Eq. (12) below.

$$|\dot{\boldsymbol{m}}| = \left(\frac{2\sigma}{2-\sigma}\right)\left(\frac{M}{2\pi R}\right)^{1/2}\left(\frac{P_{sat}-P_v}{\sqrt{T_{sat}}}\right) \qquad 12)$$

Saturation conditions are then calculated using the Clausius-Clapeyron relation with reference values corresponding to the simulation initial condition. The mass transfer rate magnitude, along with the volume fraction gradient at the interface, gives the source term for the volume fraction continuity in Eq. (13).

$$S_{\alpha_i} = |\dot{\boldsymbol{m}}_i| \cdot |\nabla\alpha| \qquad 13)$$

The volume fraction source, multiplied with the phase density, gives the source terms for the mass continuity equation in Eq (14), which sum to zero ensuring mass is conserved in Eq. (1). They must sum to zero because we are not seeding additional mass into the tank, we are changing the volume fraction of mass that is already in the tank.

$$S_c = S_{\alpha_v}\rho_v + S_{\alpha_l}\rho_l = 0 \qquad 14)$$

Finally, the source for the energy equation is the mass transfer magnitude multiplied with the latent heat of vaporization. This term is calculated using the primary phase which is liquid and given in Eq. (15).

$$S_E = S_{\alpha_l}\rho_l L = |\dot{\boldsymbol{m}}_l| \cdot |\nabla\alpha| \cdot \rho_l L \qquad 15)$$

3. *VOF Interface Sharpening*

   In general, VOF methods suffer from a diffused or smeared interface if there is significant interface motion, the physical timestep is too large, or with the addition of volume fraction (mass) sources. Due to this, additional care must be taken to prevent the interface from smearing or mass may not be conserved and nonphysical effects can occur. In STARCCM+, the High-Resolution Interface Capturing (HRIC) scheme is available, as well as a multi-step solver that applies temporal sub-cycling to the volume fraction transport equation [8]. Using the multi-step solver essentially allows using a larger global timestep, while additional sub-timesteps are used to solve the VOF equation near the interface. Additionally, a small global timestep of 4E-3 s was used in VOF case to ensure convergence.

B. Error Quantification

   To more rigorously compare deviation from experimental data, transient error metrics will be used to quantify the difference of simulation results compared to the experimental series. Russell derived metrics that measure the magnitude, and phase difference between any two functions or data series [9]. The magnitude error, ε_m, is the difference between two functions in terms of orders of magnitude. For example, when comparing two series, if the metric $\varepsilon_m = 1.0$, then series A is approximately 10 times series B over the entire dataset ($A \cong 10^{\varepsilon_m}B$). The phase error metric, ε_p, is the difference in phase between two functions in terms of percentage. A value of $\varepsilon_p = 0$ means no phase error, such as 5cos(x) and cos(x), and a value of unity is 100% out of phase, such as 5cos(x) and -cos(x). The comprehensive error, ε_c, is similar to a root mean square of the previous two metrics but scaled with $\pi/4$ [9]. The comprehensive error can be thought of as the 'average' error of the entire data series as it considers the phase difference and the relative magnitude of each datum. Russel suggests a value of $\varepsilon_c < 0.2$ for a correlation criterion between two series, in the present work a value of 0.05 was used to aid model development. These metrics provide a consistent and

robust method for comparing transient simulation and experimental data series via a single distilled value rather than a qualitative argument about which series 'looks good'. For the present work, calculations used experimental values as 'series B' and simulation results as 'series A'. This is only relevant for comparing the magnitude and phase error where the sign of the metric is important.

V. Results and Discussion

A. Transient Data Analysis

For ease of discussion, simulated cases are abbreviated and summarized in Table 2. A total of six cases are included in the present work with combinations of flow regime, phase change, and multiphase model. The GN2 pressure rise and temperature profiles were tracked during the transient simulations. Fig. 4 shows the rise in ullage pressure over time of each case along with the experimental result.

Table 2   Summary of cases and abbreviations

Case Number	Abbreviation	Multiphase Model	Flow Regime	Phase Change?
1	SST-MT	Sharp Interface	turbulent	Yes
2	LAM-MT	Sharp Interface	laminar	Yes
3	VOF-MT	Volume of Fluid	laminar	Yes
4	SST-NOMT	Sharp Interface	turbulent	No
5	LAM-NOMT	Sharp Interface	laminar	No
6	VOF-NOMT	Volume of Fluid	laminar	No

Every series has low phase error, showing good time accuracy as seen in Table 3. The values ε_p can again be interpreted as the fraction of time the simulation results are in phase with the experimental data. In terms of percentage, the
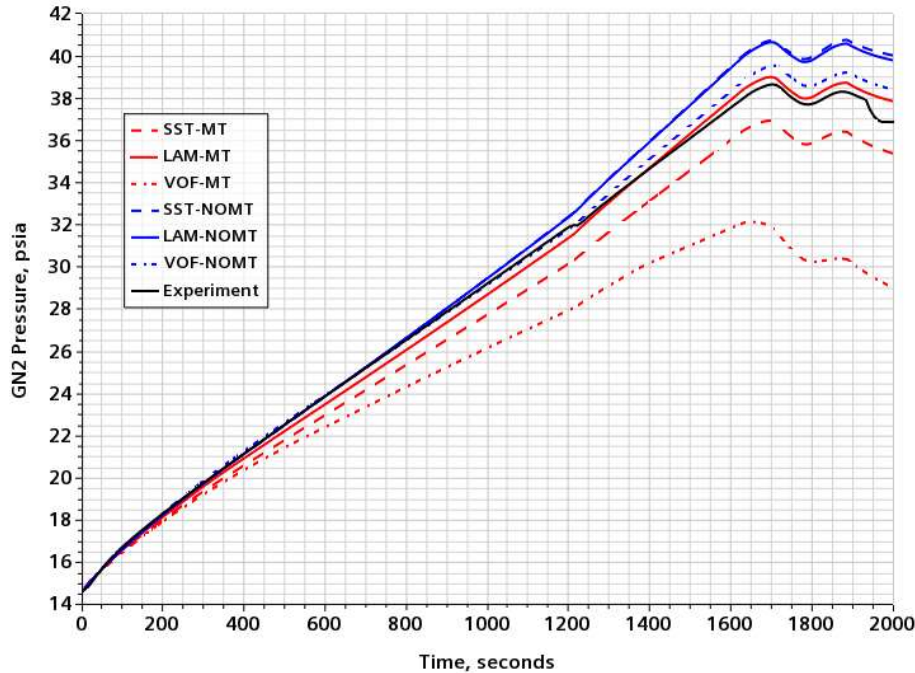

Fig. 4 N2 ullage pressure over time.

pressure trace from the SST-MT case is out of phase with the experimental data only 0.4% of the time. The low phase error for this case and others is not surprising as the experimental mass flow rate is applied directly to the CFD inlet and the ullage pressure rise is mainly due to the increased vapor mass as seen in cases without mass transfer. The ε_m values in Table 3 show that LAM-MT predicts the magnitude of the pressure trace closest to the experiment, while other cases either under or over predict. This fact is obvious from Fig. 4, but the value of error metrics is the robust

quantitative comparison between cases. The LAM-MT case predicts the pressure trace magnitude to within 1.4% of the true value across the entire experiment, an excellent result. Other SI cases also give a great prediction within 8% of the true value. All SI cases match the trend of the experiment very well with the LAM-MT matching most closely with the smallest comprehensive error.

Table 3   Pressure rise error metrics

	SST-MT	LAM-MT	SST-NOMT	LAM-NOMT	VOF-MT	VOF-NOMT
ε_m	-0.033	0.006	0.035	0.033	-0.117	-0.006
$|1 - 10^{\varepsilon_m}|$	7.3%	1.4%	8.4%	7.9%	24%	1.4%
ε_p	0.004	0.004	0.007	0.007	0.018	0.004
ε_c	0.029	0.006	0.032	0.030	0.105	0.007

It is interesting to note that when excluding mass transfer, in cases SST-NOMT and LAM-NOMT, nearly identical pressure traces are predicted, suggesting the flow is largely laminar. An estimation of the vapor region Rayleigh number is 2E6, well below the generally accepted turbulent threshold of 1E9 for natural convection problems. When mass transfer effects are included, LAM-MT follows the experimental data with excellent agreement, while SST-MT underpredicts the magnitude of the pressure rise. There are currently no sources for the k and ω transport equations for the turbulence model being used. This omission in combination with increased mixing from using a turbulence model leads to the discrepancy in pressure rise between SST-MT and LAM-MT.

VOF-NOMT matches the experiment quite well, predicting the magnitude within 1.4% across the data series. However, in VOF-MT, the magnitude is largely underpredicted by 24%. It was found the VOF-MT overpredicts the mass condensation rate, and therefore underpredicts the rise in pressure. This may be a limitation of near equilibrium applicability of the Schrage equation, but an exact cause is unclear at this time.
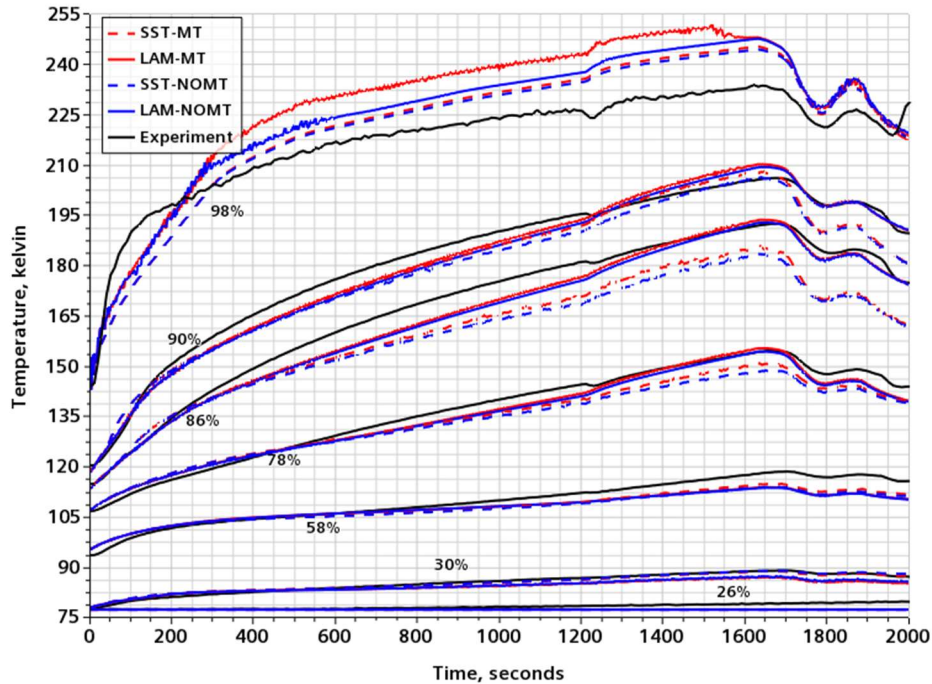

Fig. 5 Temperatures probes by fill volume over time, SI cases

The temperature stratification of the tank is plotted by fill volume in Fig. 5 for SI cases, some of the series have been removed for viewing purposes. All cases generally follow the trends of the experimental data, and the oscillations near 1800 seconds are well captured. The comprehensive error coefficients in Table 4 show that all SI cases can predict the temperature stratification with relatively low error. Temperature probes at 46%, 86%, and 98% across all cases had the largest errors, while other probes nearby, such as 94%, had very little error. This inconsistency likely stems

from the geometry simplification, uncertainty in sensor position, and the axisymmetric assumption. In the experiment, there was miscellaneous hardware and support brackets mounted internally at the top of the tank, these items were neglected in the CFD model as the size was small compared to the rest of the tank volume. These small details may
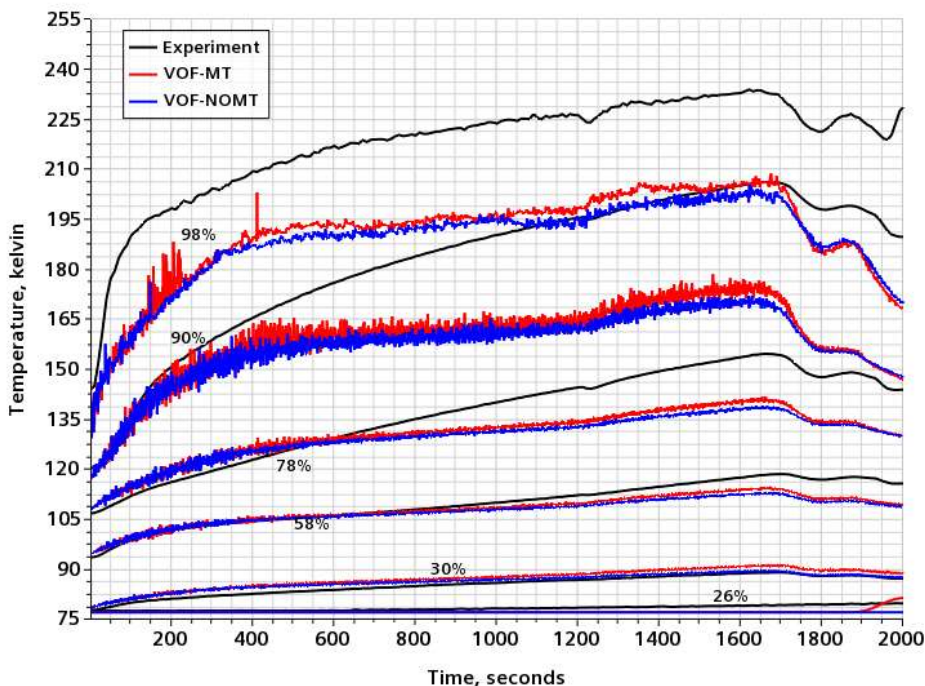

Fig. 8 Temperatures probes by fill volume over time, VOF cases

affect the local flow paths and thus shield or direct the silicon-diode sensors from the local temperature.

Temperature stratification for VOF cases is shown in Fig. 8. It can be seen that VOF cases fail to predict the temperature profile as well as the SI cases. VOF-MT and VOF-NOMT have the largest comprehensive errors and deviate from the experiment by as much as 35 K. Russell recommended an $\varepsilon_c < 0.2$ as criteria for correlation, while the authors of the present work used $\varepsilon_c < 0.05$ to develop the multiphase models [9]. VOF-MT and VOF-NOMT on average failed to meet either of these criteria for temperature stratification. From the averages of each case in Table 4, and from the comprehensive error metrics from Table 3, the LAM-MT case is the best performer as it consistently matches the experimental data with the smallest error metrics.

Table 4   Temperature probe error metrics by fill volume, ε_c

	26%	30%	46%	58%	70%	78%	82%	86%	90%	94%	98%	Mean
SST-MT	0.001	0.002	0.023	0.013	0.007	0.013	0.038	0.034	0.012	0.007	0.02	0.016
LAM-MT	0.001	0.01	0.027	0.015	0.009	0.007	0.015	0.012	0.006	0.008	0.038	0.013
SST-NOMT	0.001	0.002	0.026	0.016	0.006	0.019	0.044	0.04	0.018	0.009	0.018	0.018
LAM-NOMT	0.001	0.009	0.028	0.015	0.011	0.009	0.018	0.014	0.007	0.01	0.027	0.014
VOF-MT	0.063	0.081	0.148	0.198	0.247	0.283	0.304	0.328	0.361	0.410	0.428	0.259
VOF-NOMT	0.054	0.076	0.145	0.196	0.246	0.282	0.303	0.326	0.359	0.407	0.426	0.256

B. Energy Conservation

Due to the complexity of the model setup and the inclusion of several sources, it is important to ensure that energy and mass are being conserved throughout the domain. The change of internal energy in each region is given in Table 5, the values represent the change between the final and initial states of the simulation. The heat contributions from each source are compared to the overall change, and energy is well conserved in all cases. Q_{inlet} represents the heat added from the diffuser mass flow. Q_{liquid}, Q_{vapor}, and Q_E are the time integrals of Eqs. (6), (8), and (15) respectively.

10

In cases SST-NOMT and LAM-NOMT, a significant source of heat comes from the interface in the Q_{IL} and Q_{IV} terms. A more appropriate interface temperature in these cases would have been the local vapor temperature, such that the vapor-side temperature gradient, and therefore the heat flux Q_{IV}, is zero. However, this oversight appears to have little effect on the overall pressure trace, and the temperature probes near the interface as in Fig. 5. From Table 5, SI cases conserve energy much better compared to VOF method. This may stem from the difference of applying energy sources between the SI and VOF methods. In SI, energy sources are applied in each phase region, and there is no possibility of 'cross contamination' as the interface is a fixed temperature boundary. In VOF, the energy source is applied in VOF cells defined as having a large volume fraction gradient, i.e. near the interface. However, this does not prevent additional heat from transferring between phases, this could lead to additional numerical error in the CFD calculations. Yet in VOF-NOMT, no mass or energy sources were used, and still 12% of the internal energy injected by the diffuser inlet is unaccounted for in the final simulation state.

Table 5   Change in Energy (kJ)

	SST-MT	SST-NOMT	LAM-MT	LAM-NOMT	VOF-MT	VOF-NOMT
liquid	1144	1304	525	547	-	-
solid	2775	2782	2773	2777	2293	2214
vapor	1323	1623	1484	1608	-	-
fluid	-	-	-	-	1967	1676
$\Sigma\ Regions$	**5242**	**5709**	**4783**	**4931**	**4260**	**3890**
Q_{inlet}	4374	4374	4374	4374	4374	4374
Q_{liquid}	530	-	219	-	-	-
Q_{vapor}	-292	-	-120	-	-	-
$Q_{IL} + Q_{IV}$	619	1333	253	547	-	-
Q_E	-	-	-	-	-	-
Σ Sources	**5231**	**5706**	**4725**	**4920**	4374	4374
$\dfrac{\Sigma\ Regions}{\Sigma\ Sources} - 1$	**0.22%**	**0.04%**	**1.2%**	**0.22%**	**-33%**	**-12%**

C. Mass Transfer

The change in mass between the final and initial states is compared to the contributions from each source in Table 6, and mass is conserved globally within excellent tolerance for SI cases. Sharp interface cases without mass transfer had no significant loss of mass and are omitted. It should be noted that values presented in Table 5 and Table 6 and have been scaled by 2π to represent the entire tank, rather than the one radian section used in the axisymmetric simulations. SI cases conserve mass much better than VOF, despite SI using a much larger timestep and VOF using several sharpening techniques. It is unclear why in VOF-MT the liquid mass did not significantly increase, despite having condensed more than 1 kg of vapor, and leaving more than 6 kg of injected vapor unaccounted for. Even in the case of VOF-NOMT, 0.85 kg of mass added is lost in the final simulation state.

Table 6   Change in Mass (kg)

	SST-MT	LAM-MT	VOF-MT	VOF-NOMT
vapor region	11.37	13.19	8.02	13.64
liquid region	-	-	-0.001	-0.04
inlet source	14.45	14.45	14.45	14.45
$\dot{m}_{vap}$ source	-3.08	-1.26	-1.044	-
lost mass	-2.50E-04	2.87E-04	-6.431	-0.85
lost mass / inlet	-0.002%	0.002%	-44.51%	-5.88%

The mass transfer rates are compared in Fig. 9, again note that the values are scaled by 2π to represent the entire tank. Negative values indicate condensation from the vapor region. Using the laminar model gives a lower rate of condensation and therefore a higher rise in ullage pressure compared to the turbulent case. This is consistent with the pressure rises seen in Fig. 4. SST-MT predicts a mass transfer rate more than twice that of LAM-MT. The total mass transferred can be seen in Table 6, and again is much larger in SST-MT. Based on the pressure rises of the these two cases, Fig. 4, using a turbulence model overpredicts the condensation rate, and the total condensed mass, and therefore
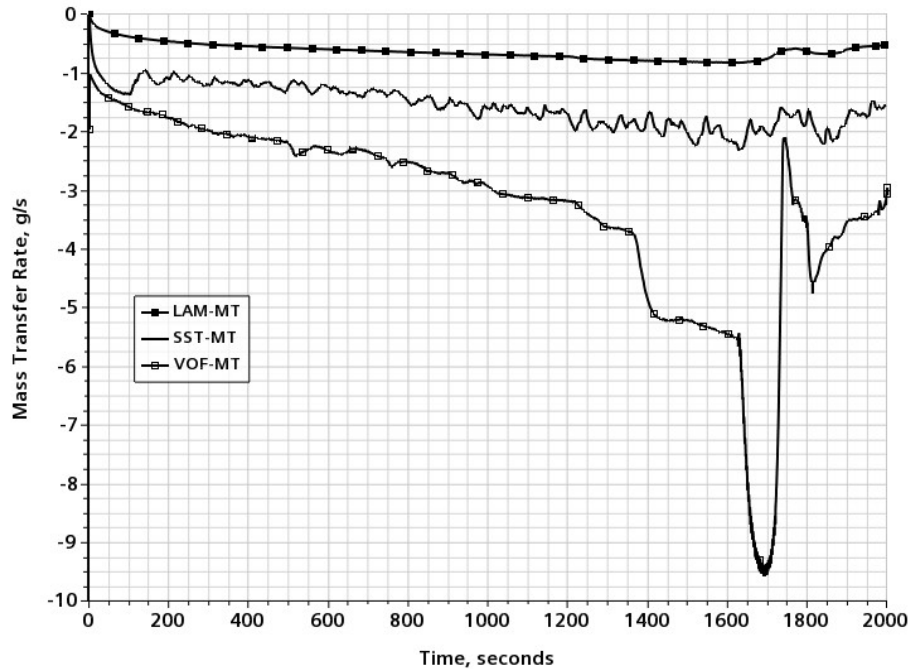

Fig. 9 Mass transfer rates

underpredicts the pressure. This discrepancy again likely stems from turbulence source terms being neglected in the current SI model and that the flow in reality is laminar. VOF-MT even further overpredicts the mass transfer rate, and is again consistent with the pressure rises in Fig. 4. At approximately 1700 s, VOF-MT predicts a condensation rate almost 10 times larger than LAM-MT. Again, this may be a sign of a limitation of using the Schrage equation in this application, but the exact reason is unknown at this time.

VI. Conclusion

Cryogenic pressurization, autogenous or otherwise, will be utilized in any space travel architecture that uses liquid propellant, this includes the current chemical rocket paradigm, and proposed nuclear thermal propulsion systems. Pressurization of liquid propellant can be used to supply rocket engine turbopumps with a subcooled liquid to prevent cavitation, as well as support on-orbit propellant transfers. Accurate predictive computational models of these processes are needed to reduce mission risk, cost, and ease the development and analysis of this technology. To address this need, two multiphase CFD models using commercially available software were developed and validated against the experimental data of a large cryogenic tank under terrestrial gravity.

The first model used the common volume-of-fluid, VOF, method and mass transfer effects were accounted for via the Schrage equation based in kinetic theory. The second approach was a sharp interface, SI, model that solves two single phase domains simultaneously and links them via an energy balance at their shared interface boundary. The SI model accurately predicts the pressure signature and temperature stratification from the EDU autogenous pressurization experiment, and conserves mass and energy within excellent tolerance. The SI model performed better than the VOF method as the SI model has lower error coefficients across the board. Using a laminar flow regime, and the sharp interface method, the magnitude of pressure rise was predicted within 1.4% over the data series. Neglecting mass transfer effects, the model still predicts the magnitude within 8%. The VOF model without mass transfer, conserved mass and energy poorly but predicted the magnitude of pressure rise was predicted within 1.4%. Using

VOF with mass transfer via the Schrage equation had a negative impact on experimental correlation, and conservation was further violated.

Using the sharp interface requires time for the analyst upfront and has much added complexity compared to VOF which works out of the box in many commercial CFD codes. However, the increase in accuracy and reduction in compute time far outweighs the drawbacks of additional setup. Each simulated SI case required approximately 8 hours of compute time on 28 CPU cores. A significant improvement over the equivalent VOF cases, which required as much as 26 times more computation time on similar hardware. We can conclude that SI model can be used as a validated tool for the design and analysis of cryogenic pressurization systems under terrestrial gravity due to its excellent agreement with experimental data, and its computation speed.

Future Work

The SI model is currently limited to stationary flat interfaces, such as pressurization under terrestrial gravity. Work is ongoing to extend the SI model to moving and arbitrary interfaces for analyses in micro-gravity, the inclusion of surface tension, and other physics. Variable material properties likely have a significant impact on pressure signatures of the EDU experiment. The specific heat for AL2219 varies significantly over the temperature range of 77 to 300 K. However, the geometry cleanup is a much larger simplification than using constant material properties. Additionally, future work should look into implementing the appropriate turbulence sources at the interface. Future cases without mass transfer effects should use the local temperature of the vapor phase, not the local saturation temperature. If mass transfer is neglected, there is no mechanism to hold the interface at saturation, and a temperature change can therefore only occur through conduction or convection.

It is currently unclear why using VOF in STAR-CCM+ tends to violate mass and energy conservation in this application even without mass and energy sources as in the VOF-NOMT case. Several orders of residual reduction on each timestep was achieved including the VOF and mass continuity equations, making it very unclear why STARCCM+ leaves a significant amount of mass unaccounted for in the final simulation state. Collaboration with the software developers is ongoing to address this issue.

References

[1]   Christian, C., Lehmann, E., Ruby, L., "Autogenous pressurization for space vehicle propulsion systems," AIAA Paper 68-626, June 1968. doi:10.2514/6.1968-626

[2]   STAR-CCM+, Simulating Transport in Arbitrary Regions Computational Continuum Mechanics, Software Package, Ver. 15.x and 16.x, Siemens

[3]   Stewart, M.. "Pressurization of a Flightweight, Liquid Hydrogen Tank: Evaporation & Condensation at a Liquid/Vapor Interface." 2017.

[4]   Hartwig, J., Plachta, D., Shirron, P., & Huget, L. "The 26th Space Cryogenic Workshop: Overview, Description of Presentations, and List of Abstracts." 2016.

[5]   NIST REFPROP, Ver. 9.1, Boulder, CO, 2013.

[6]   Mohammad Kassemi, Olga Kartuzova, Sonya Hylton, "Validation of two-phase CFD models for propellant tank self-pressurization: Crossing fluid types, scales, and gravity levels,", https://doi.org/10.1016/j.cryogenics.2017.10.019

[7]   Schrage RW. A theoretical study of interphase mass transfer. New York: Columbia University Press; 1953.

[8]   Muzaferija, S. and Peric, M., Computation of free surface flows using interface-tracking and interface-capturing methods, Nonlinear Water Wave Interaction, Computational Mechanics Publications, WIT Press, Southampton, 1999

[9]   Russell, D., "Error Measures for Comparing Transient Data," *Proceedings of the 68th Shock and Vibration Symposium,* Hunt Valley, MD, 1997